Journal of Instrumentation

Multi-guard ring TCAD simulations for different n-on-p planar silicon particle detectors

To cite this article: S. Oussalah *et al* 2021 *JINST* **16** P02034

Published by IOP Publishing for Sissa Medialab

Received: *May 26, 2020*
Revised: *December 24, 2020*
Accepted: *December 31, 2020*
Published: *February 23, 2021*

Multi-guard ring TCAD simulations for different n-on-p planar silicon particle detectors

S. Oussalah,[1] M. Mekheldi, W. Filali and E. Garoudja

Centre de Développement des Technologies Avancées,
Cité 20 août 1956, Baba Hassen, Algiers 16008, Algeria

E-mail: soussalah@cdta.dz

Abstract: This work presents a comparative study between three multi-guard ring structures that could be suitable for n-on-p silicon particle detectors for high luminosity applications. One multi-guard structure has p-type guard rings while the others have n-type guard rings with p-stop/p-spray isolation between n+ implants. The performance of the unirradiated structures are studied by increasing the fixed oxide charge density from $5 \times 10^{+10}$ to $1 \times 10^{+12}$ cm^{-2}. It's found that for two structures there is a value of oxide charge density for which the breakdown voltage is maximum while for the third structure the breakdown voltage increases with oxide charge density. The performance of the irradiated structures are evaluated with simulations up to a radiation fluence of $1 \times 10^{+16}$ 1 MeV neutron equivalent/cm^2/year (n_{eq}/cm^2) using a three trap bulk radiation model for p-type silicon substrate. Structure with n-type guard rings and p-stop isolation exhibits low leakage current and good isolation between implants while structure with p-type guard rings shows higher breakdown voltage. The breakdown voltage is enhanced by adding floating metal field plates. TCAD simulation has been used to simulate current-voltage characteristics, electron and hole concentration profiles, and electric field and potential distributions.

Keywords: Detector modelling and simulations II (electric fields, charge transport, multiplication and induction, pulse formation, electron emission, etc); Si microstrip and pad detectors; Detector design and construction technologies and materials; Solid state detectors

[1]Corresponding author.

https://doi.org/10.1088/1748-0221/16/02/P02034

2021 JINST 16 P02034

Contents

1 Introduction

Pixelated silicon particle detectors are widely used in high-energy physics experiments as those at CERN large hadron collider (LHC) and its proposed upgrade to the HL-LHC in Geneva, Switzerland. The application of this type of silicon particle detectors in the ATLAS (A Toroidal LHC ApparatuS) experiment requires a reliable performance in harsh radiation environment, which is the main test for these particle detectors [1, 2].

The radiation damage level expected during the detector lifetime implies very high bias voltages for the detector operation to maximize the signal and reduce the charge collection time [3, 4]. In most experiments at CERN's LHC structures with guard rings (GRs) are used for silicon strips and pixel detectors to improve their breakdown performance. GRs redistributes the electric field and control the potential drop from electrodes in the active area of the device to the cutting edge thus preventing breakdown along the detector edge when the device is operating at high voltages [5]–[9].

For many years, silicon detectors based on the n-on-n technology are widely used for the highly irradiated internal layers of the ATLAS experiment used for tracking of charged particles produced during the collisions of high energy protons beams produced by the LHC. Due to the high collision rates of the particles the detectors will suffer from the radiation damage, consequently the space charge becomes more negative with radiation due to the creation of negatively charged deep traps. When the space charge sign inversion (SCSI) occurs the junction moves from the back-side to the front-side and the full depletion is increased due to the increase of the net space charge density. A disadvantage of this technology is the two-sided wafer process, which requires additional masks and production steps, leading to increased costs. Planar silicon detectors based on the n-on-p technology have been under extensive studies in the HEP community in order to replace the conventional n-on-n detectors for the LHC upgrade [6]. The main advantage of this technology compared to the n-on-n technology is that all lithography process is located on one side of the wafer, and so reducing the fabrication cost. N-on-p technology has been selected as the baseline of the most silicon detectors in ATLAS Inner Tracker (ITk) of the ATLAS phase-II upgrade detector at the HL-LHC. Nevertheless these devices are more complex as they need a good isolation between n-type implants because of the positive charges that are present in the silicon dioxide (SiO_2) layer. These positive charges attract free electrons and induce a thin layer negatively charged at the Si/SiO_2 interface [10]. This layer can form a conductive path between the different electrodes and hence short them, increases crosstalk, and leads to unwanted parasitic leakage current if no isolation mechanism were introduced. This insulation is achieved by two kinds of blank surface implant, named p-spray or p-stop [11]. P-spray is a lightly doped layer over the wafer surface and p-stop is a heavily doped p+ implant between the n-type implants.

In the literature many multi-guard design for n-on-p technology are reported [6, 7]–[12, 13]. We estimated that Koybasi et al. [7] have proposed an interesting and simple multi-guard geometry for silicon particle detectors for high luminosity applications. Based on this structure, this work presents a comparative study between three different multi-guard silicon particle detectors based on the n-on-p technology with and without p-stop/p-spray isolation between the GRs in order to assess their electric behavior when operating at high luminosity applications. The structures have been simulated with and without radiation damage using Silvaco™ Technology Computer Assisted Design (TCAD) simulation software. The surface radiation damage is modeled in the simulator by introducing an amount of oxide charge density and interface traps and the bulk radiation damage is modeled by a three level traps model [14, 15].

2 Device structures and TCAD simulation

2.1 Device structures

Figure 1 shows a schematic cross-section of three different silicon detector structures. The structures are based on high-resistivity p-type silicon substrate, the doping concentration and the thickness are $5 \times 10^{+11}$ cm^{-3} and of 300 µm, respectively. The last pixel is surround by GRs with different spacing and width between them. The number of GRs is fixed to 8, with an implant width are 5 to 30 µm with the largest at the outer side of the structure. Distance between them varying from 20 to 35 µm. The guard rings represent a dead zone in pixel sensors, meaning no particle is detected close to the structure. More detail about the structure can be found in reference [7]. The pixel is n+ type with a peak concentration of $1 \times 10^{+18}$ cm^{-3} and a depth of 1.5 µm. The oxide thickness is 1 µm and the oxide charge density varies from $5 \times 10^{+10}$ to $1 \times 10^{+12}$ cm^{-2}. Figure 1a shows the structure proposed in reference [7] that has p-type GRs while the figure 1b and figure 1c show structures with n-type GRs with p-stop [16] implant or with p-spray [17] layer implanted at the surface to ensure isolation between n+ implants. In this study, the first structure is called pGR while the others are called nGR-pst and nGR-psp, referring to the GRs type doping and the isolation type between the GRs.

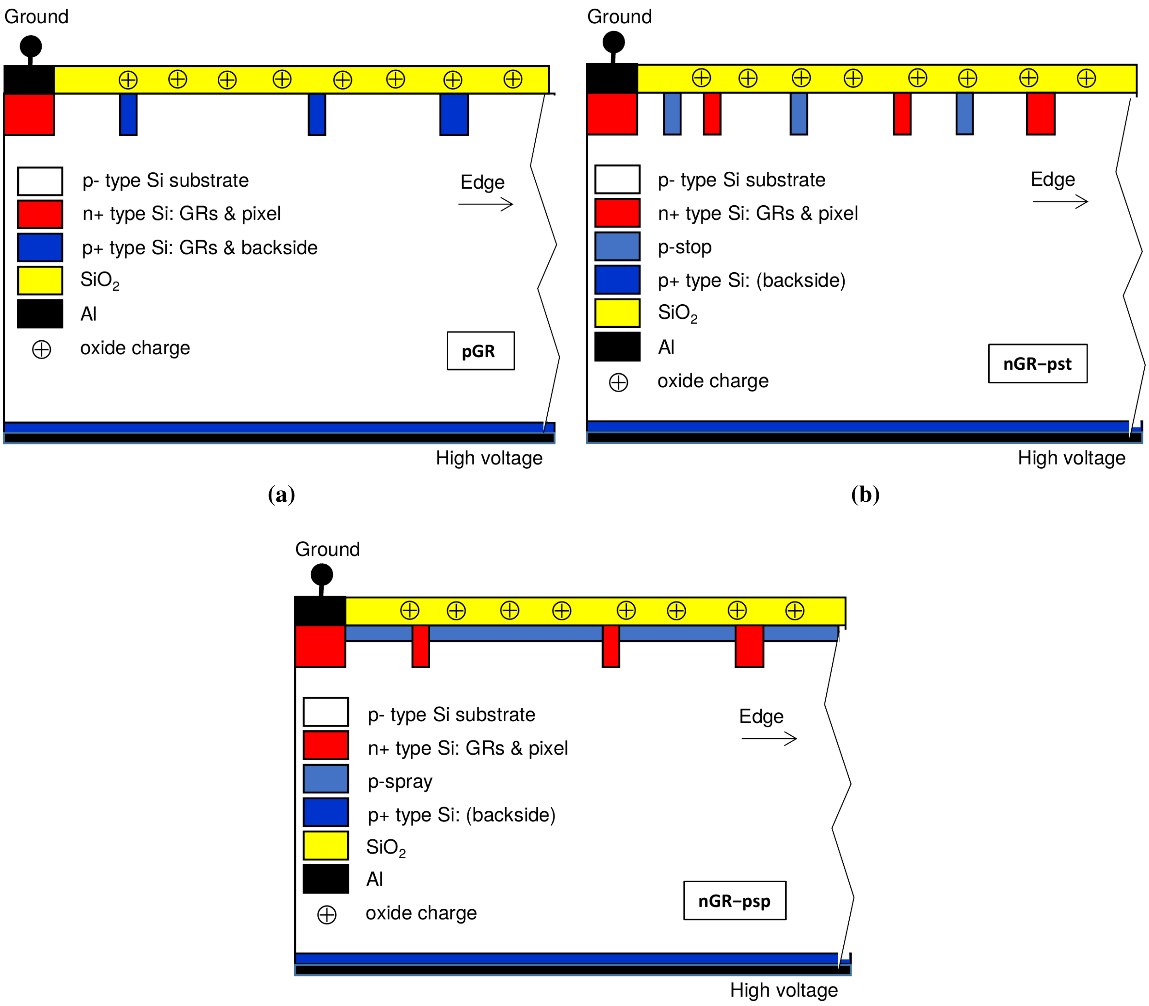

Figure 1. Cross-sectional schematic of the simulated p-type substrate silicon detector structures (a) with p-type GRs [7], (b) with n-type GRs with p-stop isolation, and (c) with n-type GRs with p-spray isolation.

2.2 TCAD simulation

2.2.1 Physical models

Numerical Simulation by computer is a powerful tool that allows researchers and engineers to better understand the physics of material and electronic devices, achieve optimized design, and save times. Simulation results presented in this work are carried out using Atlas from Silvaco's TCAD software [18]. Atlas is a 2D and 3D finite element device simulator that performs DC, AC, and transient analysis for silicon and other semiconductor material-based devices. Atlas enables the conception, characterization and optimization of semiconductor devices under different constraints (electrical, optical, and thermal) for a wide range of microelectronics process technologies. The electronic device takes a grid mesh made of discrete elements as an input structure and solves the Poisson's equation along with carrier continuity and drift-diffusion equations for electrons and holes at each point of the grid mesh to calculate the electrical, physical and optical properties. Atlas is able to calculate current, capacitance, potential and electric field distributions and carrier mobility inside the device. For the transient mode, the displacement current is also calculated [19]. The physical models such as Schokley-Read-Hall and Auger recombinations accounting for low- and high-level injection effects, concentration and field dependent mobility, and band gap narrowing used in our simulation are included in the default bipolar physical model of Atlas. Impact ionization is a crucial and important phenomena to be considered when semiconductor device works at high electric field. In Atlas, the Selberherr's physical model [20] is used among other models to predict the impact ionization effect in semiconductor devices that reflects the generation of free carriers (electrons, holes) mechanism resulting the avalanche breakdown. The avalanche breakdown is analyzed by determining where and at what bias voltage the ionization integral exceeds unity that corresponds to infinite carrier multiplication. The junction breakdown voltage is accurately predicted and the junction curvature effects causing higher electric fields at the device corners are included in the program. The electric field lines, potential contours, current flow lines, and impact ionization generation rates are plotted by Tonyplot. Thereby, the location where the breakdown occurs can be precisely identified. In our simulation, the refined mesh is located at the p-n/p-p junctions and at the Si/SiO_2 interface to ameliorate the accuracy of the results with an optimized height and width of 0.2 and 0.5 µm, respectively. Moreover, the number of mesh points was chosen as a compromise between simulation accuracy and computation time.

2.2.2 Bulk radiation damage model

The principle source of radiation damage in semiconductor detectors is from the non-ionizing-energy-loss (NIEL). It's expressed in terms of 1 MeV neutron equivalent for silicon (1 MeV n_{eq}/cm^2). Radiation damage introduces defects in the bulk of the material that modify its behavior. The primary effects of the radiation bulk damage are the inversion of the substrate n-type material, an increase in leakage current, and a reduction of the charge collection efficiency due to increasing number of traps. Different TCAD radiation damage model exist and consist in defining a set of defect states, characterized by their concentration and type (i.e. whether they are an acceptor or a donor), location (energy level) in the band gap, electron and hole capture cross-sections (σ_n, σ_p). Moscatelli et al. from the University of Perugia [14] have proposed a new radiation trap model to describe bulk radiation damage caused by proton collisions irradiation in p-type silicon substrate grown by floating zone (FZ) technique. The model consists of the generation of three traps in the bandgap of the silicon substrate, two acceptors and one donor. The density of traps is predicted to increase linearly with radiation fluence Φ, so for each trap an introduction rate (η) is defined as $\eta = N\Phi^{-1}$, where N is the trap density. The detail of the trap model is presented in tables 1 and 2.

Table 1. Parameters of the three trap bulk radiation damage model proposed by University of Perugia [14] used in our simulations for fluences up to $7 \times 10^{+15}$ neq/cm^2. The energy levels are given with respect to the conduction band (E_C) or the valence band (E_V).

Bulk defect	Energy level (eV)	σ_n (1/cm^2)	σ_p (1/cm^2)	η (1/cm)
Acceptor	$E_C - 0.42$	1.0×10^{-15}	1.0×10^{-14}	1.613
Acceptor	$E_C - 0.46$	7.0×10^{-15}	7.0×10^{-14}	0.9
Donor	$E_V + 0.36$	3.23×10^{-13}	3.23×10^{-14}	0.9

2021 JINST 16 P02034

Table 2. Parameters of the three trap bulk radiation damage model proposed by University of Perugia [14] used in our simulations for fluences in the range $7 \times 10^{+15}$–$1.5 \times 10^{+16}$ neq/cm^2. The energy levels are given with respect to the conduction band (Ec) or the valence band (Ev).

Bulk defect	Energy level (eV)	σ_n (1/cm^2)	σ_p (1/cm^2)	η (1/cm)
Acceptor	$E_C - 0.42$	1.0×10^{-15}	1.0×10^{-14}	1.613
Acceptor	$E_C - 0.46$	3.0×10^{-15}	3.0×10^{-14}	0.9
Donor	$E_V + 0.36$	3.23×10^{-13}	3.23×10^{-14}	0.9

2.2.3 Surface radiation damage model

A protective coating useful as a passivation layer for semiconductor devices incorporates a layer of several 100 nm of SiO_2 grown onto the silicon wafers in a high temperature oxygen atmosphere. However SiO2 layer is positively charged due to technological processes and induces defects both in it volume (N_{OX}) and at Si/SiO_2 interface (N_{IT}). For a non-irradiated detectors the oxide charge density is estimated about $5 \times 10^{+10}$ cm^{-2} for a good quality of SiO_2 layer [10]. The oxide charge density is known to vary linearly with exposed radiation fluence up to saturation. The oxide charge saturation varies within a range of $1 \times 10^{+12}$ and $3 \times 10^{+12}$ cm^{-2} depending on the oxide thickness and crystal orientation [21, 22]. Values reported in literature are not very uniform due to strong process dependence. As a consequence, electrons are accumulated at the Si/SiO_2 interface of the silicon detectors due to this positive charge. Accordingly the n+ implants can be shorted and the generated signal would spread over several pixels.

Table 3. Parameters of oxide charge ($N_{OX} = 10^{+12}$ cm^{-2}) and interface trap density (N_{IT} = 80% of N_{OX}) introduced in the surface damage model [14] and used in our simulations. The energy levels are given with respect to the conduction band (E_C) or the valence band (E_V).

Interface defect	Energy level (eV)	Concentration (1/cm^2)
Acceptor	$E_C - 0.4$	40% of $N_{IT} = 0.8\,N_{OX}$
Acceptor	$E_C - 0.6$	60% of $N_{IT} = 0.8\,N_{OX}$
Donor	$E_V + 0.6$	100% of $N_{IT} = 0.8\,N_{OX}$

The surface model developed by Moscatelli et al. [14] consists of introducing physical parameter values (N_{OX} and N_{IT}) extracted from experimental measurements on gated diodes and MOS capacitors realized on p-type substrates after gamma irradiations. For the interface trap states description, they considered the combined effect of one donor interface trap at $E_T = E_V + 0.6$ eV from the valence band [14] and two acceptor interface traps at $E_T = E_C - 0.4$ eV and at $E_T = E_C - 0.6$ eV from the conduction band following the findings in [23, 24]. For the donor concentration N_{IT}, 100% of donor traps are allocated at $E_T = E_V + 0.6$ eV. For a given acceptor concentration N_{IT}, 60% of acceptors traps are allocated at $E_T = E_C - 0.6$ eV, while the remaining 40% are allocated at $E_T = E_C - 0.4$ eV according to [23, 24]. Moscatelli et al. [14] considered an extensive analysis using different values of the ratio N_{IT}/N_{OX} to match the experimental data. The ratio $N_{IT}/N_{OX} = 0.8$ is found to match correctly the experimental data for a heavily irradiated structure. Therefore, in this study, we take into account the damage inflicted on the SiO_2 layer by varying N_{OX} and N_{IT} as shown in table 3. We assume that oxide charge saturates at 10^{+12} cm^{-2}.

2021 JINST 16 P02034

3 Results and discussion

3.1 Pre-irradiation simulation

In our recent work [16], we compared the pGR and nGR-pst structures for some geometrical parameters before irradiation like substrate doping and thickness, guard ring doping and depth, and oxide thickness and charge density. We found that breakdown voltage is not influenced by oxide thickness variation. On the other hand for both structures we observed a decrease of the breakdown voltage with an increase of the deviation of oxide charge density from a specific value. However, breakdown voltage increases continuously with oxide charge density for nGR-psp as shown in reference [17]. P-spray concentration must compensate the surface electron layer that is formed as a consequence of the positive charge trapped in the oxide mainly at the saturation. So, thanks to TCAD simulation, this compensation can be visualized by drawing a cuteline just under the Si/SiO_2 interface as shown in figure 2b. A we can see, the doping concentration of p-spray of $4 \times 10^{+16}\,\mathrm{cm}^{-3}$ is sufficient to compensate the surface electron layer and hence to ensure isolation between n+ implants. Figure 3 shows that for p-spray doping concentration of $1 \times 10^{+16}\,\mathrm{cm}^{-3}$ the potential at the edge of the sructure is nearly the same as for the pixel however for a concentration of $4 \times 10^{+16}\,\mathrm{cm}^{-3}$ the potential is distributed over the guard rings.

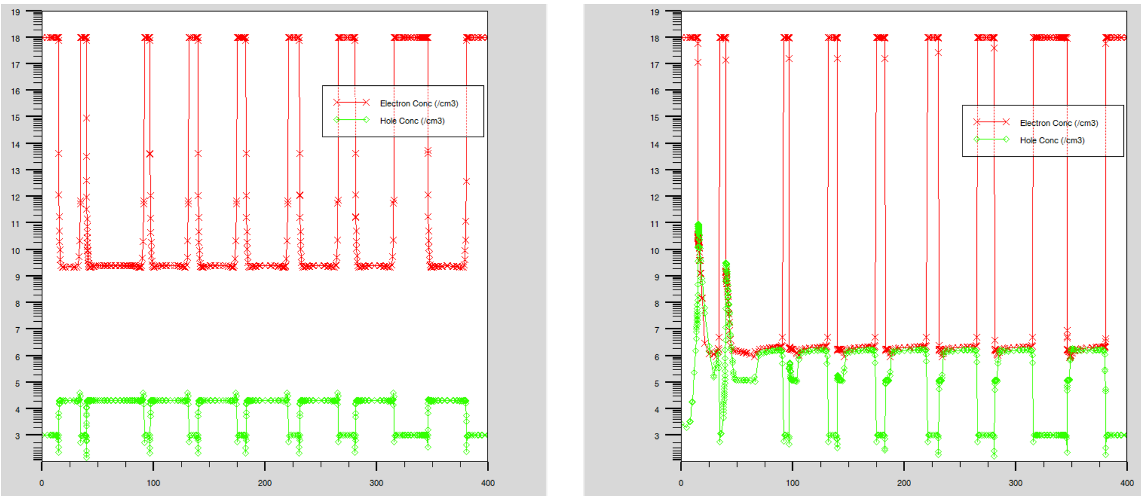

(a) (b)

Figure 2. Simulated electron (red curve) and hole (green curve) concentration distribution along to the surface of nGR-psp structure at 0.1 µm under the surface for p-spray doping concentration of (a) $1 \times 10^{+16}\,\mathrm{cm}^{-3}$ and (b) $4 \times 10^{+16}\,\mathrm{cm}^{-3}$. The structure is reverse biased at 500 V and the oxide charge density is $1 \times 10^{+12}\,\mathrm{cm}^{-2}$.

The reverse current-voltage characteristics of the multi-guard structures with different oxide charge density are shown in figures 4a, 4b, and 4c for pGR, nGR-pst, and nGR-psp, respectively. The maximum values of breakdown voltage are about 1200 V and 400 V for pGR and nGR-pst structures attributed to the oxide charge density of $4 \times 10^{+11}\,\mathrm{cm}^{-2}$ and $6 \times 10^{+11}\,\mathrm{cm}^{-2}$, respectively. We note that simulation is performed with Synopsys TCAD in reference [10] that can explain the difference for the optimum value of oxide charge density [25]. At an oxide charge density of $1 \times 10^{+12}\,\mathrm{cm}^{-2}$ the breakdown voltage is 700 V, 280 V and 400 V for of pGR, nGR-pst, and nGR-psp, respectively.

2021 JINST 16 P02034

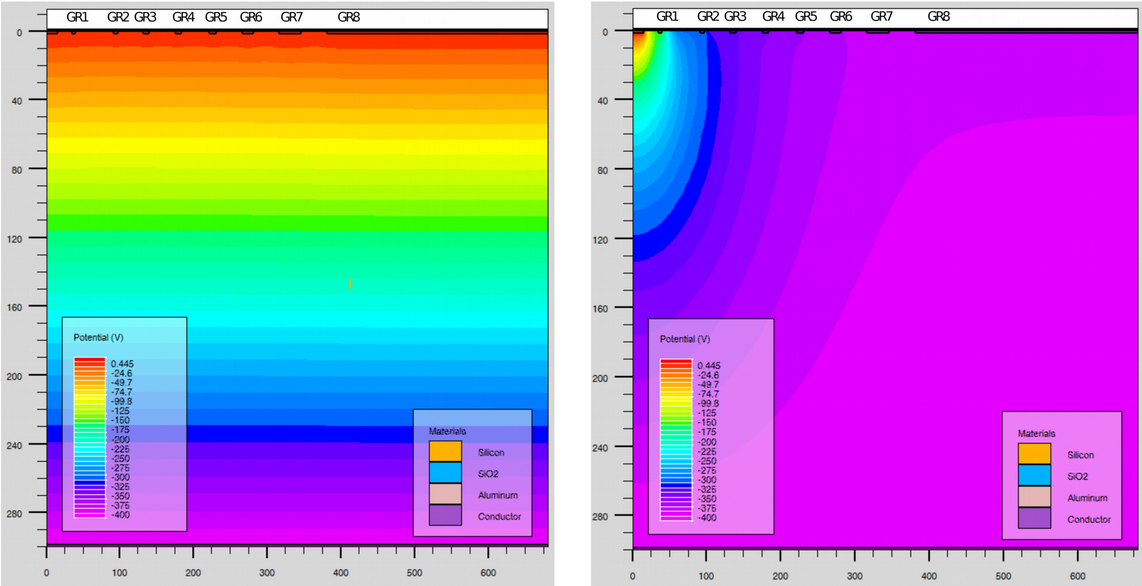

(a) **(b)**

Figure 3. Simulated potential profile in the bulk of nGR-psp structure for p-spray doping concentration of (a) $1 \times 10^{+16}\,\mathrm{cm}^{-3}$ and (b) $4 \times 10^{+16}\,\mathrm{cm}^{-3}$. The structure is reverse biased at 500 V and the oxide charge density is $1 \times 10^{+12}\,\mathrm{cm}^{-2}$.

pGR shows better electrical performance than the others structures in term of breakdown voltage when oxide charge saturates. The Breakdown voltage increases continuously with oxide charge density for nGR-psp structure since the build-up charge in the oxide will compensate the p-spray doping concentration.

Figure 5 and figure 6 show the simulation results for the potential and the electric field distributions at a depth of 0.1 μm under the Si/SiO_2 interface for the structures pGR and nGR-pst, respectively. At each figure two values of oxide charge density are presented $5 \times 10^{+10}\,\mathrm{cm}^{-2}$ (left) and $1 \times 10^{+12}\,\mathrm{cm}^{-2}$ (right). The structures are reverse biased just below the breakdown voltage at 400 V and 250 V for pGR and nGR-pst, respectively. With this potential distribution, pGR and nGR-pst structures are able to sustain reverse biases exceeding 1100 V and 400 V as shown in figure 4a and figure 4b, respectively. For lower or higher oxide charge density, the device structure performance are degraded.

At low oxide charge density the conductivity of the device silicon surface is low and therefore the majority of the potential drops at the pixel and at the first GR or the first p-stop implant facing the pixel resulting in higher electric field peaks as shown in figures 7a and 7c and figures 8a and 8c for the structures pGR and nGR-pst, respectively. As the surface conductivity of the device increases the potential drop is distributed uniformly over the guard rings, which results in an increase in the slope of potential drop at each GR or p-stop implant. When the optimum value of oxide charge density is reached, i.e. 4–6 $\times 10^{+11}\,\mathrm{cm}^{-2}$, and corresponding to the maximum breakdown voltage the electric field peaks distribution is more or less uniform. The increased amount of oxide charge density results in a steep potential drop at each lateral p-/p+ boundaries as shown in figure 7d and figure 8d. This is due to the interruption of the electron channel resulting in higher electric field

2021 JINST 16 P02034

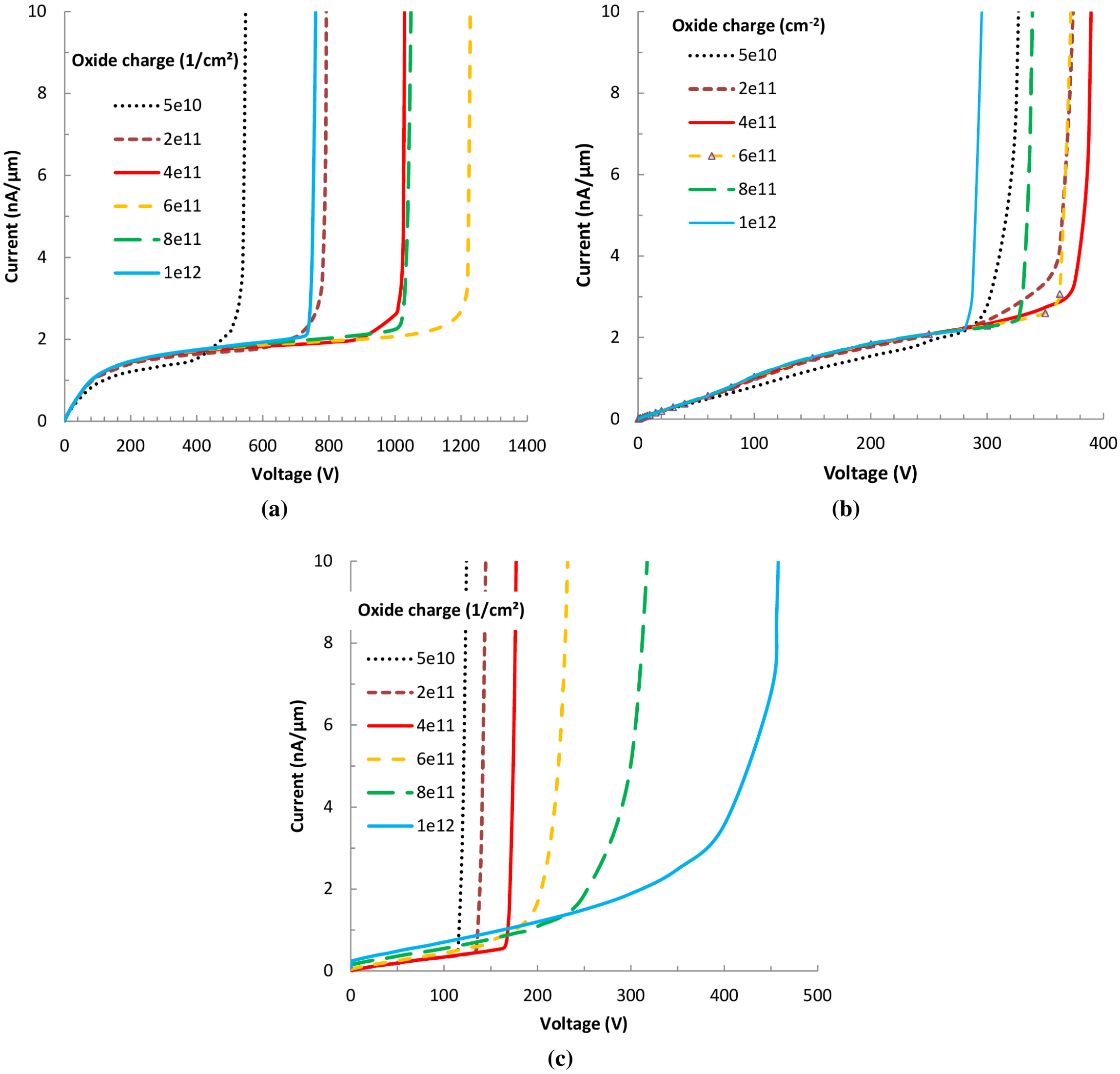

Figure 4. Reverse I-V characteristics as a function of oxide charge density for (a) pGR, (b) nGR-pst, and (c) nGR-psp structures, respectively. A decrease of the breakdown voltage with an increase of the deviation of oxide charge density from $6 \times 10^{+11}$ cm^{-2} and from $4 \times 10^{+11}$ cm^{-2} for pGR and nGR-pst, respectively. The breakdown voltage increases continuously with oxide charge density for nGR-psp structure.

peaks and therefore a lower breakdown voltage as shown in figure 7b and figure 8b for pGR and nGR-pst structures, respectively. Higher breakdown voltage values of pGR structure compared to nGR-pst structure are due to the field distribution uniformity even at oxide charge saturation as shown in figure 7b.

P-spray layer with adequate doping and depth is used to compensate the accumulating electrons to keep the inter-pixel isolation at sufficient levels. As the oxide charge density increases, the p-spray layer is partially compensated and the electrical field between p-spray and n+ implant is decreased [26]. Consequently, the breakdown voltage of silicon sensors using a p-spray inter-pixel isolation technique increases with oxide charge.

2021 JINST 16 P02034

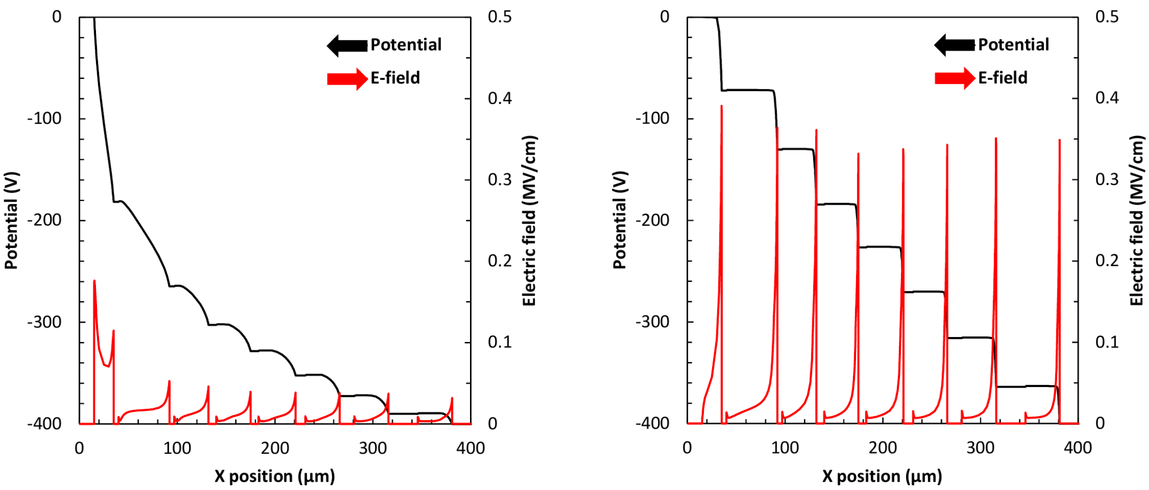

(a) (b)

Figure 5. Simulated potential drop and electric field distributions at a depth of 0.1 μm under Si/SiO2 interface of pGR device for oxide charge density of (a) $5 \times 10^{+10}$ cm^{-2} and (b) $1 \times 10^{+12}$ cm^{-2}, respectively. The bias voltage is 400 V, just below the breakdown voltage.

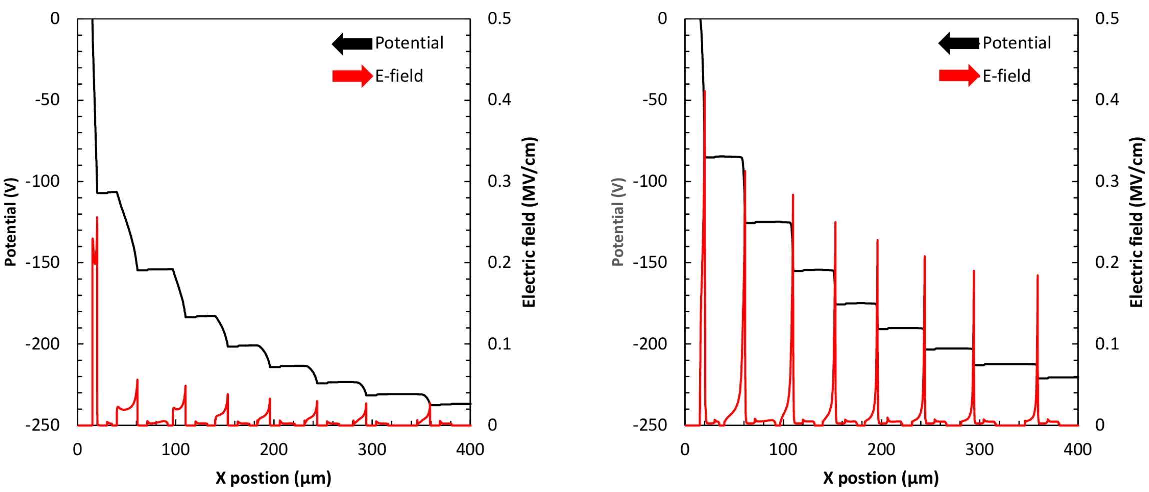

(a) (b)

Figure 6. Simulated potential drop and electric field distributions at a depth of 0.1 μm under Si/SiO2 interface of nGR-pst device for oxide charge density of (a) $5 \times 10^{+10}$ cm^{-2} and (b) $1 \times 10^{+12}$ cm^{-2}, respectively. The bias voltage is 250 V, just below the breakdown voltage.

2021 JINST 16 P02034

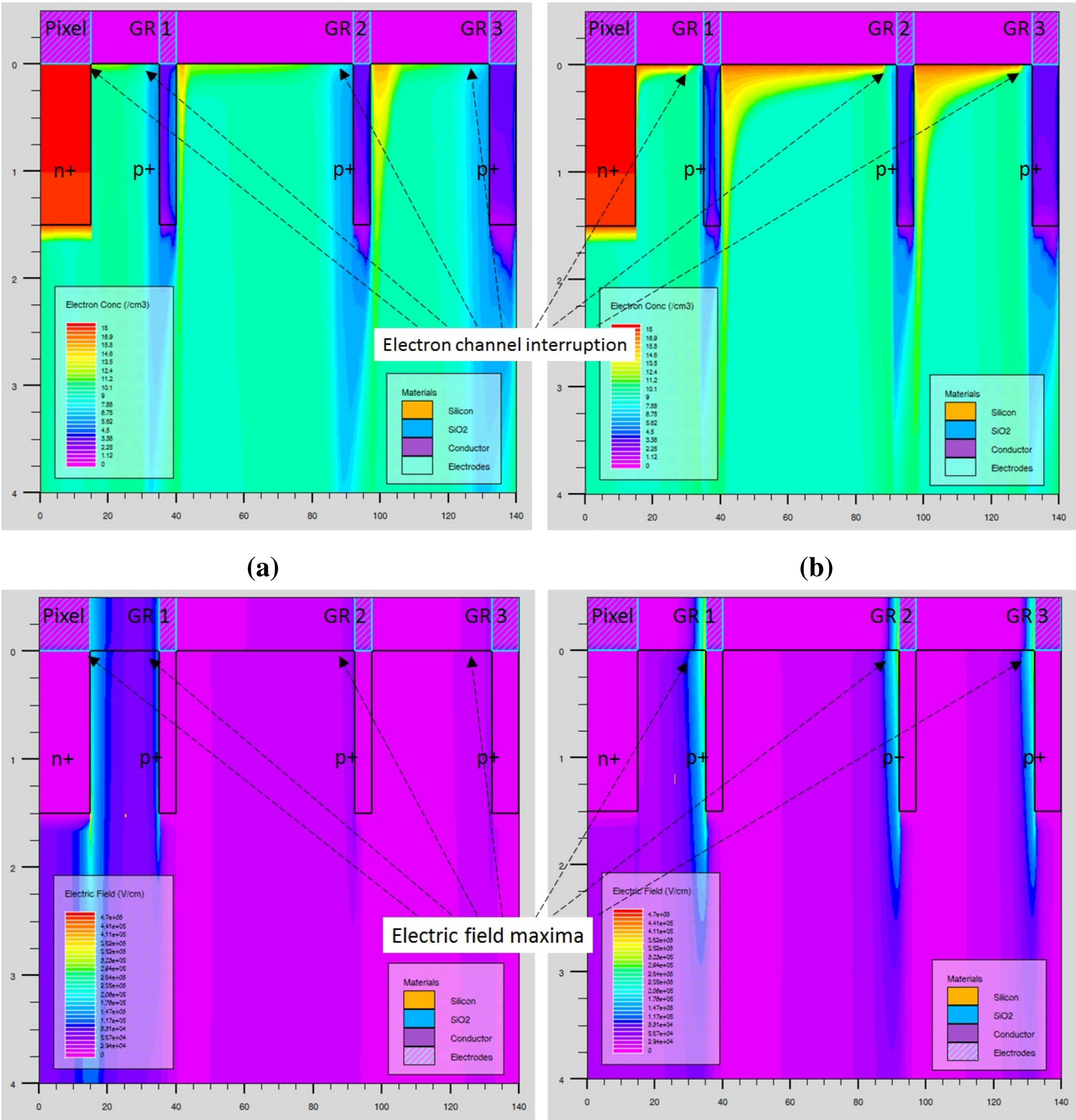

Figure 7. Simulated (a) and (b) electron concentration distribution and (c) and (d) electric field contours along to the surface of pGR structure for the first three GRs at 4 µm under the surface. The oxide charge density is $5 \times 10^{+10}\,\mathrm{cm}^{-2}$ (left) and $1 \times 10^{+12}\,\mathrm{cm}^{-2}$ (right) and the bias voltage is 400 V, just below the breakdown voltage.

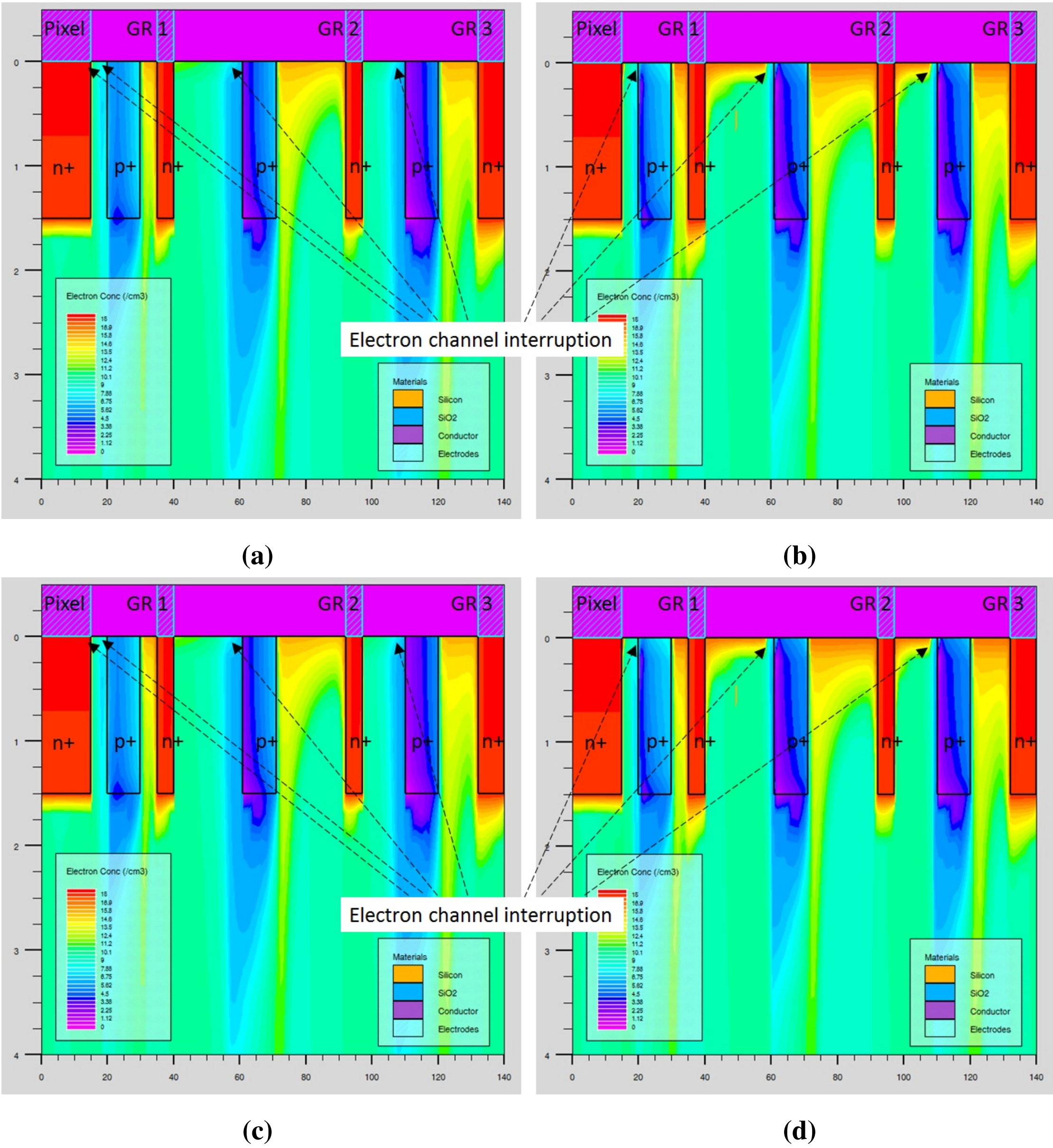

Figure 8. Simulated (a) and (b) electron concentration distribution and (c) and (d) electric field contours along to the surface of pGR structure for the first three GRs at 4 µm under the surface. The oxide charge density is $5 \times 10^{+10}\,\mathrm{cm}^{-2}$ (left) and $1 \times 10^{+12}\,\mathrm{cm}^{-2}$ (right) and the bias voltage is 250 V, just below the breakdown voltage.

3.2 Post-irradiation performance

The electrical performances of the irradiated multi-guard structures have been evaluated with simulation using the three trap bulk radiation model and the surface damage model presented in table 1 and table 2, respectively. The simulation has been performed for fluence from $1 \times 10^{+14}$ to $1 \times 10^{+16}\,\mathrm{n_{eq}/cm^2}$ and for charge oxide density varying from $5 \times 10^{+10}$ to $1 \times 10^{+12}\,\mathrm{cm}^{-2}$. The evolution of the breakdown voltage versus the oxide charge density as a function of fluence density for both structures is simulated. The evolution is always the same, i.e. there is a value of oxide charge for which the breakdown voltage is maximum for pGR and nGR-pst structures while the breakdown

2021 JINST 16 P02034

voltage increases with the oxide charge for the different fluences for the nGR-psp structure. As one can see, the breakdown behavior degrades significantly with radiation for all structures as shown in figure 9. At a fluence of $1 \times 10^{+16}\,\mathrm{n_{eq}/cm^2}$ and for an oxide charge of $1 \times 10^{+12}\,\mathrm{cm^{-2}}$, the pGR, nGR-pst, and nGR-psp structures are able to survive only up to bias voltage of 100–150 V. The breakdown voltages for both structures is not high enough for very high luminosity applications, so further improvements are needed. However, nGR-pst structure shows better behavior in term of leakage current than the others structures when oxide charge saturation takes place. The simulation of the electron concentration distribution for both structures at a depth of 0.1 µm under the surface at a fluence of $1 \times 10^{+16}\,\mathrm{n_{eq}/cm^2}$ and for oxide charge density of $1 \times 10^{+12}\,\mathrm{cm^{-2}}$ is reported in figure 10. These simulation results can give us information on the isolation capacity between the pixel and the guard rings. As we can see nGR-pst structure presents lower electron concentration about $10^{+5}\,\mathrm{cm^{-3}}$ compared to the others structures.

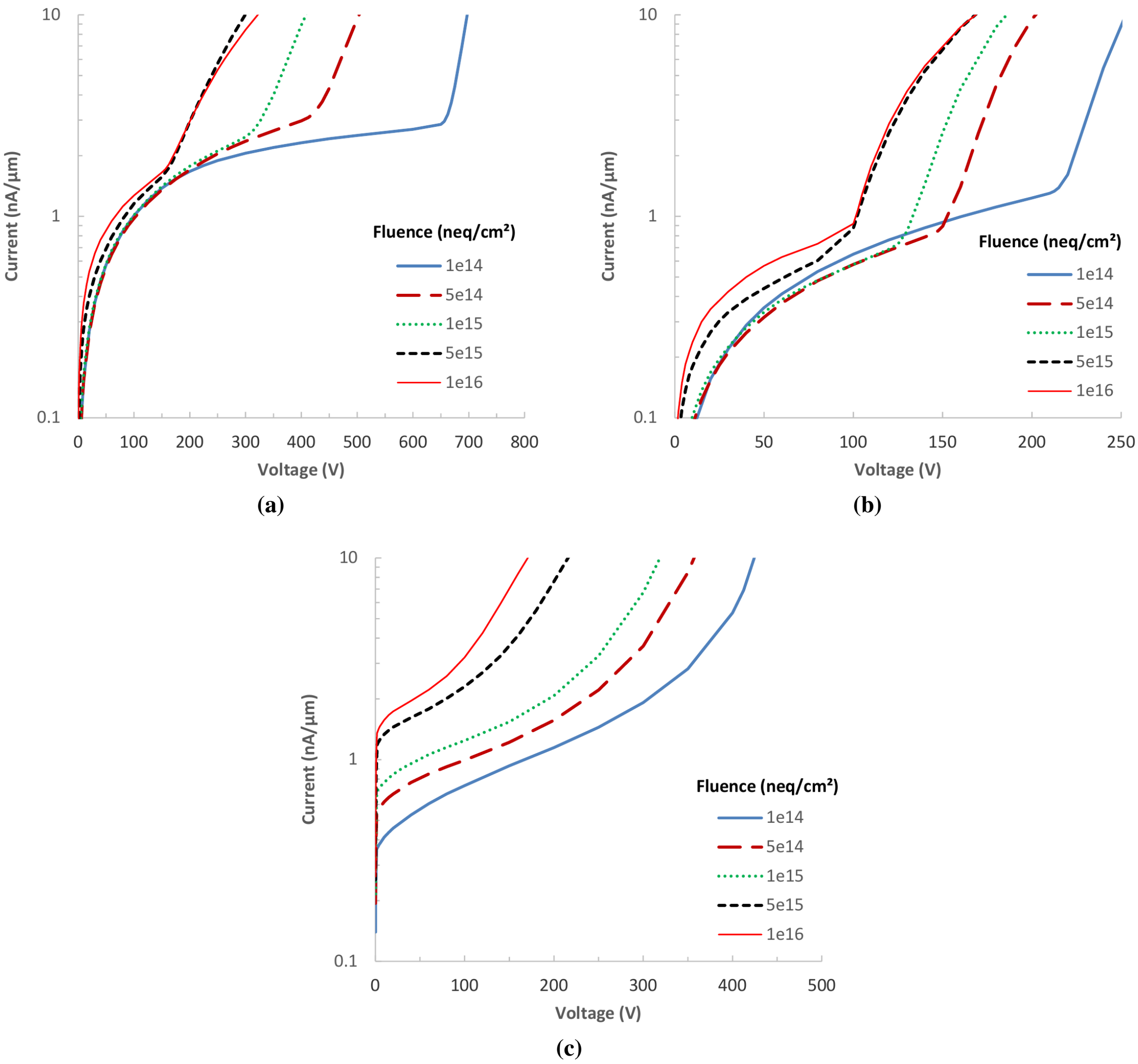

Figure 9. Reverse I-V characteristics at different fluences ranging from $1 \times 10^{+14}$ to $1 \times 10^{+16}\,\mathrm{n_{eq}/cm^2}$, for (a) pGR, (b) nGR-pst, and (c) nGR-psp structures, respectively. The oxide charge density is $1 \times 10^{+12}\,\mathrm{cm^{-2}}$.

2021 JINST 16 P02034

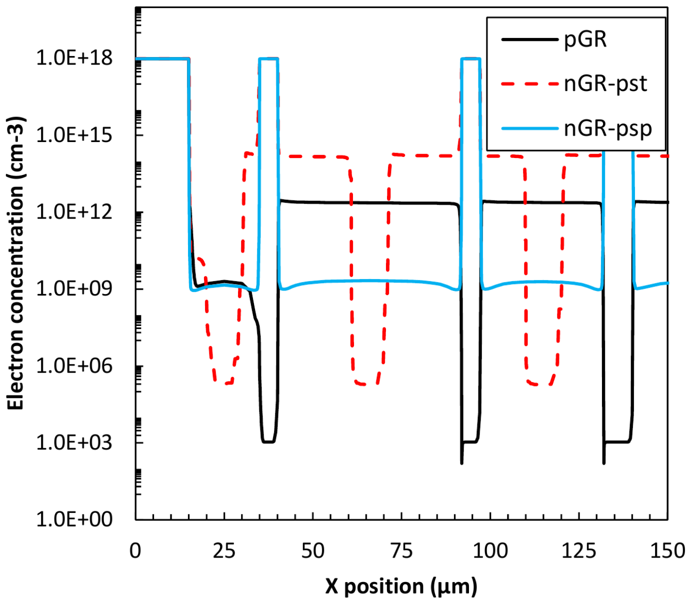

Figure 10. Simulated electron concentration distribution at a depth of 0.1 μm from Si/SiO_2 interface at a fluence of $1\times10^{+16}$ n_{eq}/cm^2 for pGR structure (black line), nGR-pst structure (red line), and nGR-psp structure (blue line). The oxide charge density is $1\times10^{+12}$ cm^{-2} and the structures are reverse biased at 100 V.

3.3 Breakdown voltage improvement

Field plates (FP) can reduce the electric field after irradiation. They are at the same potential of the implant regions they are in contact with. Therefore, they are at lower potential than the underlying silicon as the potential drops from the pixel towards the structure edge. This forms a negatively biased p-MOS structure, which results in accumulation of holes at the Si/SiO_2 interface. Since the electric field peaks are located at the lateral p/p+ boundaries facing the pixel where the electron channel is interrupted and the potential drops, FPs are positioned on the p+ implants, i.e., p-type guard rings and p-stop implants for pGR and nGR-pst structures, respectively. Contrariwise, the electric field peaks are located at the lateral n+/p boundaries facing the edge of the nGR-psp structure, so FPs are positioned on the n+ implants, i.e., n-type guard rings. Figure 11 shows the simulated pGR and nGR-pst structures featuring field plates extending towards the active region and the simulated nGR-psp structure featuring field plates extending towards the edge.

Figure 12 shows the I-V characreristices as a function of oxide charge density for (a) pGR, (b) nGR-pst, nGR-psp structures with filed plates, respectively. We remark that the breakdown increases continuously with oxide charge density contrary to what was found for structures without PFs (see figure 4). At an oxide charge of $1\times10^{+12}$ cm^{-2}, the breakdown voltage is approximately 1200 V, 600 V, and 800 V for pGR, nGR-pst, and nGR-psp structures, respectively.

Figure 13 shows the electron density and electric field distributions around the two innermost guard rings of the (a) pGR and (b) nGR-pst structures with FPs at a reverse bias taken just below the breakdown voltage for a radiation fluence of $1\times10^{+15}$ n_{eq}/cm^2 and an oxide charge of $1\times10^{+12}$ cm^{-2}. The electron layer induced by the positive oxide charge sees its density drop dramatically at the Si/SiO_2 interface regions under the FPs to the left of the p-implants due to the lower electrostatic

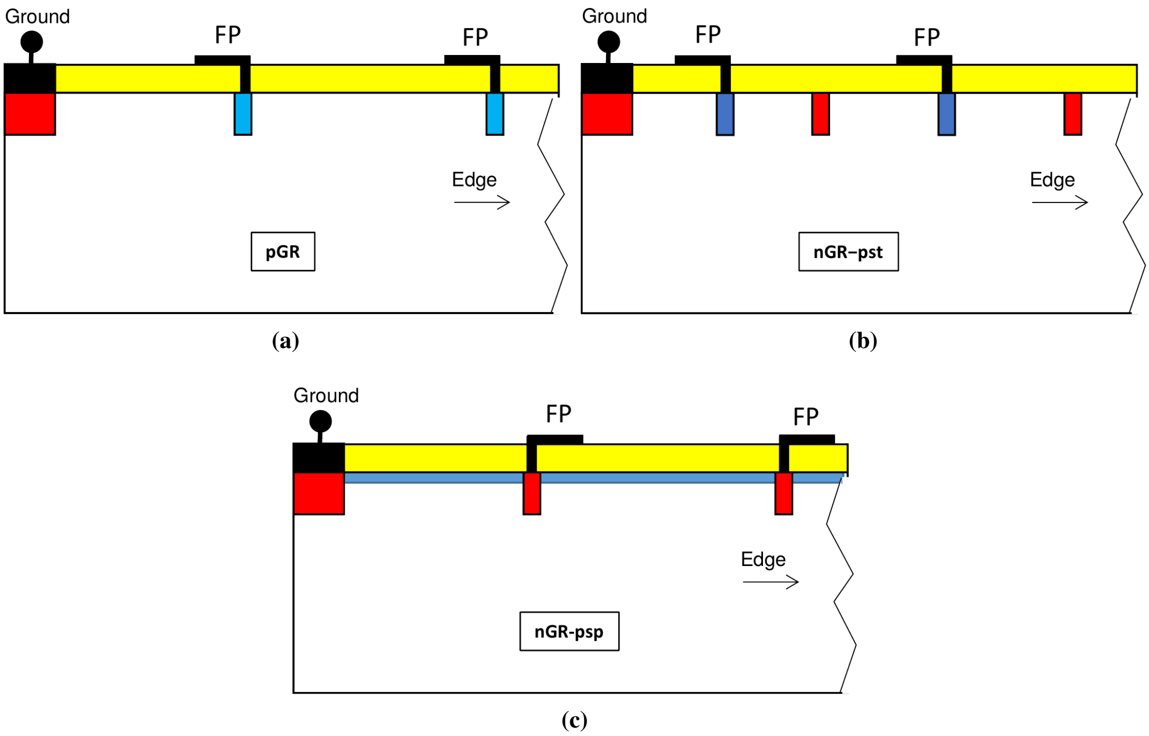

Figure 11. Cross-section of the simulated (a) pGR, (b) nGR-pst, and (c) nGR-psp structures with field plates, respectively.

potential of the FPs relative to the silicon surface. In addition to the electric field peaks located at the p/p+ boundary facing the active region, FPs create secondary electric field peaks in silicon underneath their left edges where the potential drop starts. The electric field will be distributed over more spots with a lower peak value at each spot and therefore the breakdown voltage will be improved.

The simulation of the I-V characteristics of the multi-guard ring structures with FPs as a function of radiation fluence for an oxide charge density of $1 \times 10^{+12}$ cm^{-2} are shown in figure 14. For pGR structure, a breakdown voltage of 800 V and 300 V have been attained after fluences of $1 \times 10^{+15}$ n_{eq}/cm^2 and $1 \times 10^{+16}$ n_{eq}/cm^2, respectively. For nGR-pst structure, a breakdown voltage of 350 V and 170 V have been attained after fluences of $1 \times 10^{+15}$ n_{eq}/cm^2 and $1 \times 10^{+16}$ n_{eq}/cm^2, respectively. For nGR-psp structure, a breakdown voltage of 600 V and 250 V have been attained after fluences of $1 \times 10^{+15}$ n_{eq}/cm^2 and $1 \times 10^{+16}$ n_{eq}/cm^2, respectively. As we can see, FPs improves breakdown voltage. A further study on the optimization of the length of the FPs combined to the oxide thickness permits to improve more the breakdown voltage of the structures.

Table 4 resumes the simulation results for the breakdown voltage for the pGR, nGR-pst, and nGR-psp structures with and without FPs for two values of fluence. The breakdown voltage is enhanced by adding floating metal field plates by a factor of two.

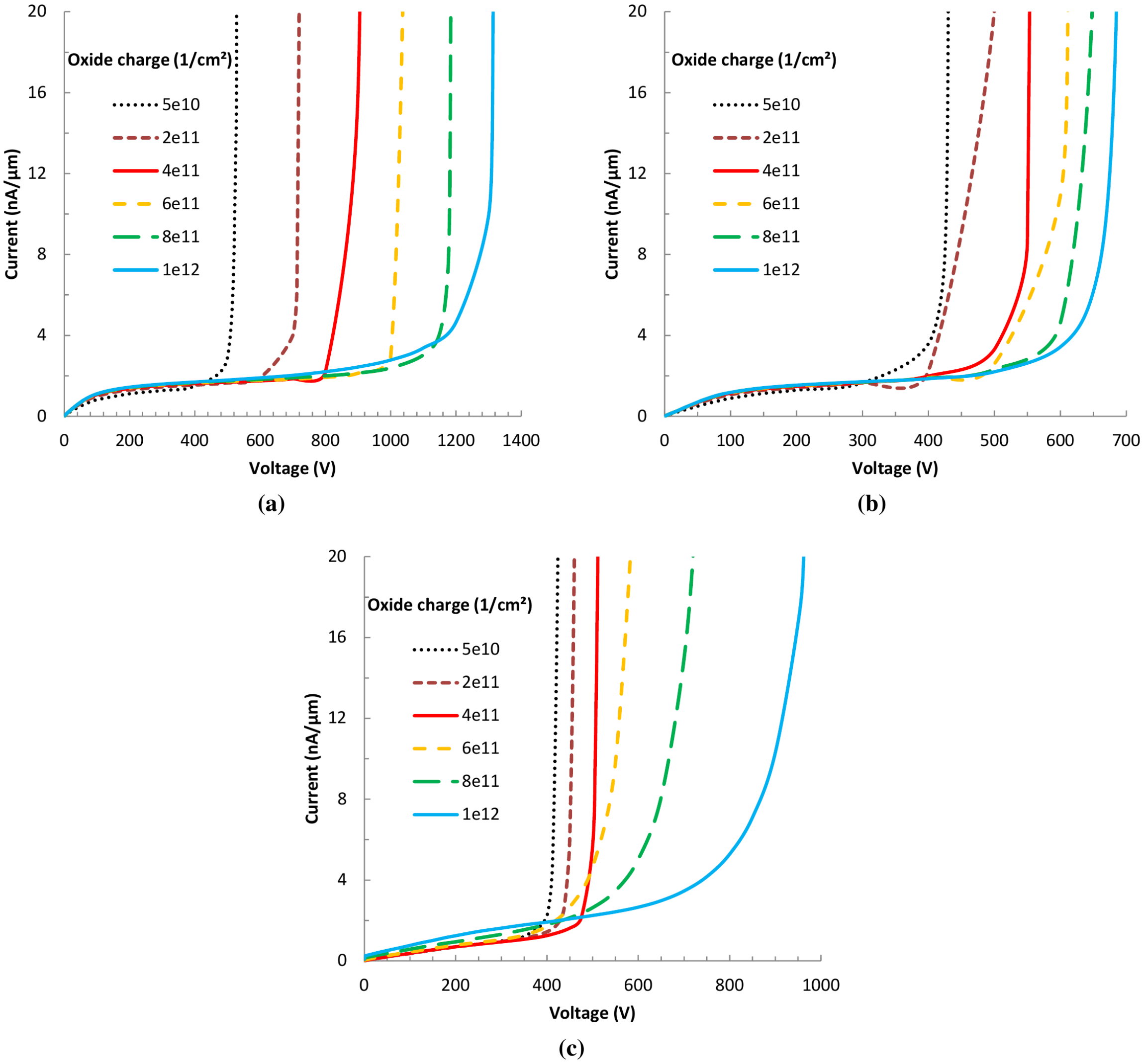

Figure 12. Breakdown behavior as a function of oxide charge density for (a) pGR, (b) nGR-pst, and (c) nGR-psp structures with field plates, respectively. The breakdown voltage increases continuously with oxide charge density for all structures.

Table 4. Breakdown voltage for pGR and nGR-pst structures with and without FPs.

Fluence	$1 \times 10^{+15}$ n_{eq}/cm^2		$1 \times 10^{+16}$ n_{eq}/cm^2	
Structure	Without FPs	With FPs	Without FPs	With FPs
pGR	300 V	800 V	150 V	300 V
nGR-pst	125 V	350 V	<100 V	170 V
nGR-psp	250 V	600 V	100 V	250 V

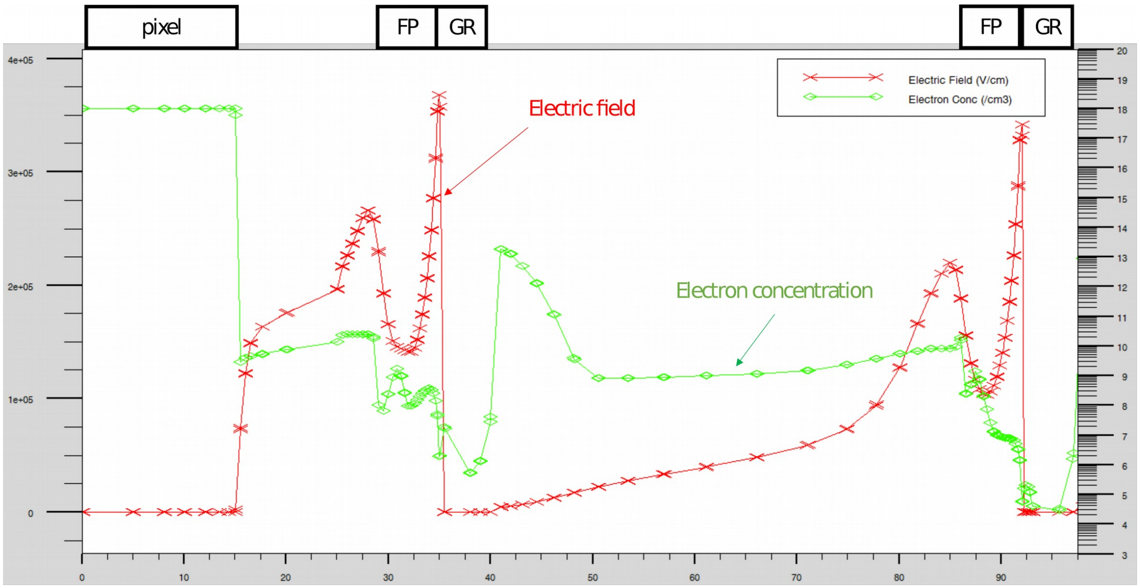

(a)

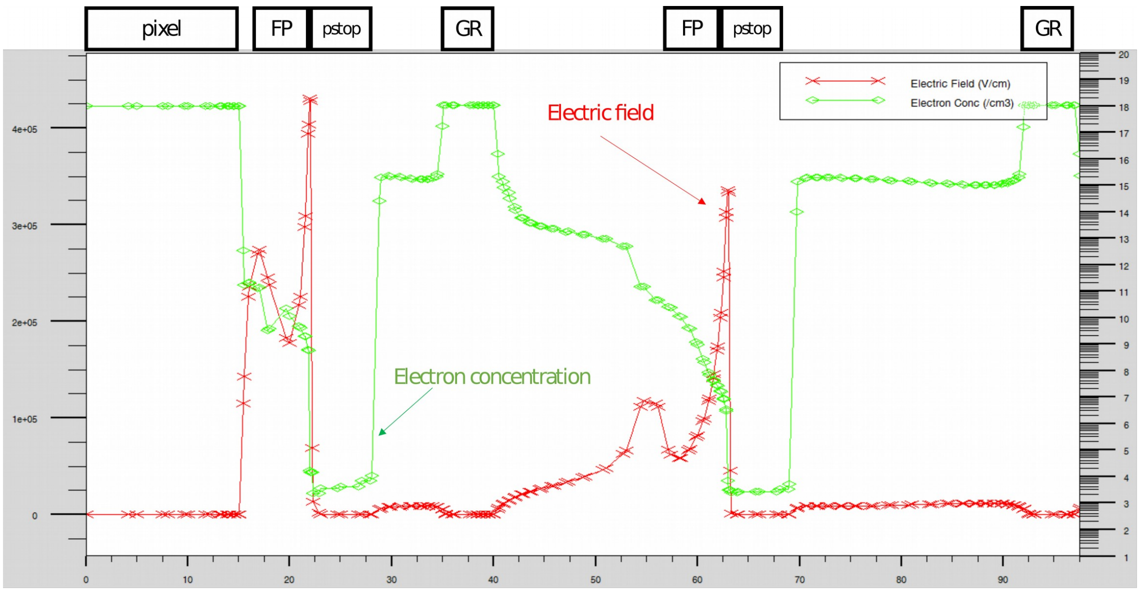

(b)

Figure 13. Simulated electron concentration and electric field distributions around the two innermost guard rings at a depth of 0.1 μm under Si/SiO$_2$ interface at a fluence of $1 \times 10^{+15}$ n$_{\mathrm{eq}}$/cm^2 and for oxide charge density of $1 \times 10^{+12}$ cm^{-2} of (a) pGR and (b) nGR-pst structures, respectively. The bias voltage is taken just below the breakdown voltage.

2021 JINST 16 P02034

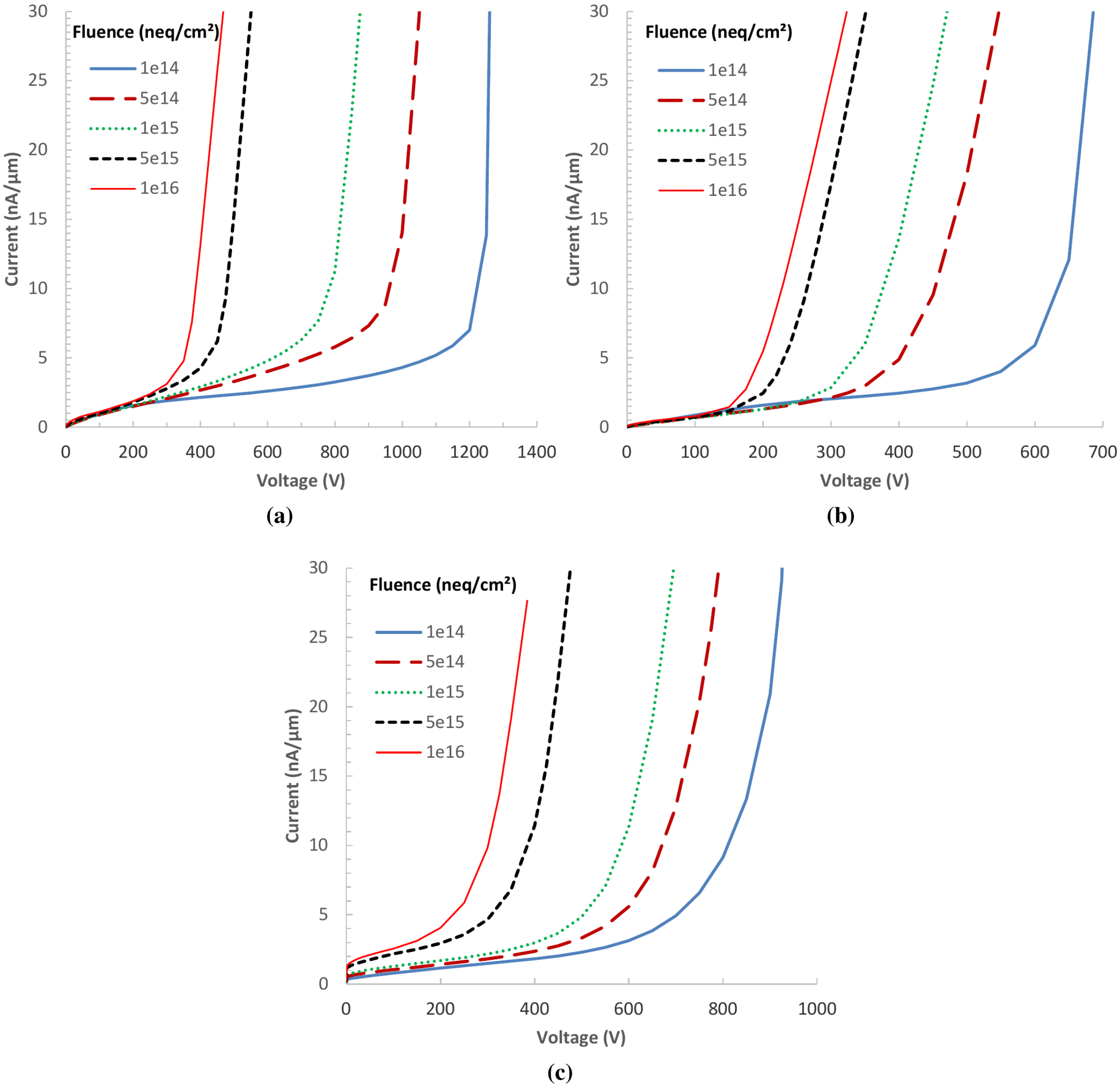

Figure 14. Breakdown behavior as a function of fluences for (a) pGR, (b) nGR-pst, and (c) nGR-psp structures with field plates, respectively. The oxide charge density is $1 \times 10^{+12}$ cm^{-2}.

4 Conclusion

In summary, we have evaluated the electrical performances of three different high-voltage silicon detectors based on n-on-p technology dedicated to high-energy physics experiments using Atlas (Silvaco) TCAD tool. One structure has p-type guard rings while the others have n-type guard rings with p-stop/p-spray isolation between n+ implants. Without radiation, we observed a decrease of the breakdown voltage with an increase of the deviation of oxide charge density from $6 \times 10^{+11}$ cm^{-2} and from $4 \times 10^{+11}$ cm^{-2} for structures with p-type guard rings and n-type guard rings with p-stop isolation, respectively. For these oxide charge optimum values the structure featuring p-type guard rings can withstand reverse bias voltages above 1200 V while the structure featuring n-type guard rings with p-stop isolation can withstand only 400 V. Structure with n-type guard rings with p-spray isolation shows a continuous increase of breakdown voltage with oxide charge density. With radiation, it was found that with increasing fluence density from $1 \times 10^{+14}$ to $1 \times 10^{+16}$ n_{eq}/cm^2 breakdown voltage decreases significantly for all structures. The structure with p-type guard rings exhibits higher values of breakdown voltage than the others structures. The structure with n-type guard rings with p-stop isolation shows better behavior in term of leakage current when oxide charge saturation takes place. Moreover, isolation between implants is more assured by n-type guard rings structure with p-stop isolation. The breakdown voltage is improved by a factor of two when adding floating field plates on the p-type implants pointing towards the active region for structures with p-type guard rings and n-type guard rings with p-stop isolation. For the structure with n-type guard rings with p-spray isolation the floating field plates must be pointed towards the edge. We think that the optimisation of oxide thickness, length of the field plates, and the doping and depth of the isolation layer can contribute to improve the performances of the detectors.

References

[1] A. Affolder et al., *Silicon detectors for the sLHC*, *Nucl. Instrum. Meth. A* **658** (2011) 11.

[2] L. Evans and P. Bryant, *LHC Machine*, 2008 *JINST* **3** S08001.

[3] G. Lindstrom, M. Moll and E. Fretwurst, *Radiation hardness of silicon detectors: A challenge from high-energy physics*, *Nucl. Instrum. Meth. A* **426** (1999) 1.

[4] J. Becker, *Signal development in silicon sensors used for radiation detection*, Ph.D. Thesis, University of Hamburg, Hamburg Germany (2010).

[5] V. Mishra, V.D. Srivastava and S.K. Kataria, *Role of guard rings in improving the performance of silicon detectors*, *Pramana* **65** (2005) 259.

[6] M. Benoit, A. Lounis and N. Dinu, *Simulation of guard ring influence on the performance of ATLAS pixel detectors for inner layer replacement*, 2009 *JINST* **4** P03025.

[7] O. Koybasi, G. Bolla and D. Bortoletto, *Guard ring simulations for n-on-p silicon particle detectors*, *IEEE Trans. Nucl. Sci.* **57** (2010) 2978.

[8] V. Chmill et al., *Study of various high voltage protection structures for reduction of the insensitive region of silicon sensors designed for extreme radiation tolerance*, 2011 *JINST* **6** C01062.

[9] V. Eremin et al., *Operation of voltage termination structure in silicon n^+-p-p^+ detectors with Al_2O_3 field isolator grown by Atomic Layer Deposition method*, 2018 *JINST* **13** P11009.

[10] T.P. Ma and P.V. Dressendorfer, *Ionizing radiation effects in MOS devices and circuits*, Wiley-Interscience, Hoboken NJ U.S.A. (1989).

[11] S. Chatterji, M. Singla, W.F.J. Mueller and J.M. Heuser, *Optimization of various isolation techniques to develop low noise, radiation hard double-sided silicon strip detectors for the CBM Silicon Tracking System*, *IEEE Trans. Nucl. Sci.* **60** (2013) 2254 [arXiv:1211.6286].

[12] C. Gallrapp et al., *Performance of novel silicon n-in-p planar Pixel Sensors*, *Nucl. Instrum. Meth. A* **679** (2012) 29 [arXiv:1112.5395].

[13] L.E. Gkougkousis, *Recent achievements of the ATLAS Upgrade Planar Pixel Sensors R&D Project*, in proceedings of the *2014 IEEE Nuclear Science Symposium and Medical Imaging Conference (NSS/MIC)*, Seattle, WA, U.S.A., 8–15 November 2014, pp. 1–7.

2021 JINST 16 P02034

[14] F. Moscatelli, D. Passeri, A. Morozzi, R. Mendicino, G.F. Dalla Betta and G.M. Bilei, *Combined Bulk and Surface Radiation Damage Effects at Very High Fluences in Silicon Detectors: Measurements and TCAD Simulations*, *IEEE Trans. Nucl. Sci.* **63** (2016) 2716 [arXiv:1611.10138].

[15] D. Djamai et al., *Performance of n-on-p planar pixel sensors with active edges at high-luminosity environment*, *Eur. Phys. J. Plus* **135** (2020) 101.

[16] M. Mekheldi, S. Oussalah, A. Lounis and N. Brihi, *Simulation of Guard Ring Type Effects on the Electrical Characteristics of n-on-p Planar Silicon Detectors*, *J. Nano- Electron. Phys.* **11** (2019) 04008.

[17] M. Mekheldi, S. Oussalah, A. Lounis and N. Brihi, *Comparison of electrical performances of two n-in-p detectors with different implant type of guard ring by TCAD simulation*, *Results Phys.* **6** (2016) 80.

[18] Silvaco Inc., *ATLAS User's Manual. Device Simulation Software*, Silvaco, Inc., Santa Clara CA U.S.A. (2016).

[19] M.S. Sze and M.K. Lee, *Semiconductor Devices Physics and Technology*, Wiley-Interscience, New York NY U.S.A. (2012).

[20] S. Selberherr, *Analysis and Simulation of Semiconductor Devices*, Springer, New York NY U.S.A. (1984) [https://doi.org/10.1007/978-3-7091-8752-4].

[21] E.H. Nicollian and J.R. Brews, *MOS (Metal Oxide Semiconductor) Physics and Technology*, Wiley-Interscience, New York NY U.S.A. (2002).

[22] L. Rossi, P. Fischer, T. Rohe and N. Wermes, *Pixel detectors. From Fundamentals to applications*, in *Particle Acceleration and Detection*, Springer, Berlin Germany (2006).

[23] J. Zhang, *X-ray radiation damage studies and design of a silicon pixel sensor for science at the XFEL*, Ph.D. Thesis, University of Paris Diderot, Paris France (2018).

[24] F.R. Palomo Pinto, M. Moll, J. Schwandt, E.G. Villani, Y. Gurimskaya and R. Millán, *TCAD Device Simulations of Irradiated Silicon Detectors*, *PoS* **Vertex2019** (2020) 051.

[25] M. Bomben, *Silicon trackers for high luminosity colliders*, Ph.D. Thesis, University of Paris Diderot, Paris France (2018).

[26] J.L. Beyer, *Optimisation of Pixel Modules for the ATLAS Inner Tracker at the High-Luminosity LHC*, Ph.D. Thesis, University of Munich, Munich Germany (2019).

2021 JINST 16 P02034